Field-emission properties of novel palladium nanogaps for surface conduction electron-emitters

Field-emission properties of novel palladium nanogaps for surface conduction electron-emitters

Hsiang-Yu Lo[1]**, Yiming Li**[1,3]**, Hsueh-Yung Chao**[1]**, Chih-Hao Tsai**[2] **and Fu-Ming Pan**[2]

[1] Department of Communication Engineering, National Chiao Tung University, Hsinchu, Taiwan
[2] Department of Materials Science and Engineering, National Chiao Tung University, Hsinchu, Taiwan

E-mail: ymli@faculty.nctu.edu.tw

Abstract
We explore novel nanometer-scale gaps with different widths in palladium (Pd) thin-film strips using hydrogen absorption under high-pressure conditions and different temperatures. Both the experimental measurement and numerical calculation are conducted to examine the electron conduction properties of the newly proposed surface conduction electron-emitters (SCEs). It is shown that this novel structure exhibits a high emission efficiency, so that a low turn-on voltage of 40 V for an SCE with a 30 nm nanogap is obtained. A calibrated model is adopted to predict the effects of the emitter thickness and different material work functions on emission current with different width of nanogaps. It is found that the heightened thickness increases the emission current. However, it tends to saturate for smaller nanogaps. The decrement of work function is proportional to the increase in emission current, which is independent of the width of nanogap.

(Some figures in this article are in colour only in the electronic version)

1. Introduction

Diverse applications of electrodes with nanometer separation have recently been of great interest, such as for molecular electronics [1, 2], biosensors [3], and vacuum microelectronics [4]. However, most relevant research on nanogaps is only in its infancy, because complicated fabrication processes cannot be modeled exactly. One of the up-to-date applications of nanogaps is the surface conduction electron-emitter (SCE) for flat-panel displays (FPDs). The surface conduction electron-emitter display (SED) is a new type of FPD based upon SCEs [5–7]. SEDs have the advantage of having a simple structure, high image quality, good color, wide viewing angle, quick response time, as well as low power consumption. The critical process step for fabricating an SCE is to create a nanofissure on a line electrode where the electron emission occurs. Thus, the

nanogap fabrication technique is rather complicated and expensive. Also, computer simulation of SCE has not been clearly drawn yet. A multiple scattering model for the electron emission mechanism of the SCE has been proposed [8]. However, it does not consider the full three-dimensional (3D) fields and charged particles for electron emission in SED, and this model is only valid in an emitter with a coplanar cathode. As a result, the study into obtaining high emission current, high emission efficiency, and stable fabrication for SCE has become an interesting issues in recent years.

In this paper, we study the field-emission properties of a palladium (Pd) nanogap. The sample is fabricated by a simple and well-controlled high-pressure hydrogen absorption treatment method [9]. Theoretically, we formulate a calibrated model for analyzing the field-emission efficiency of this proposed structure of a Pd thin-film emitter with various nanogaps ranging from 30 to 90 nm under different conditions. A 3D finite-difference time-domain particle-in-cell (FDTD-

---

[3] Author to whom any correspondence should be addressed.
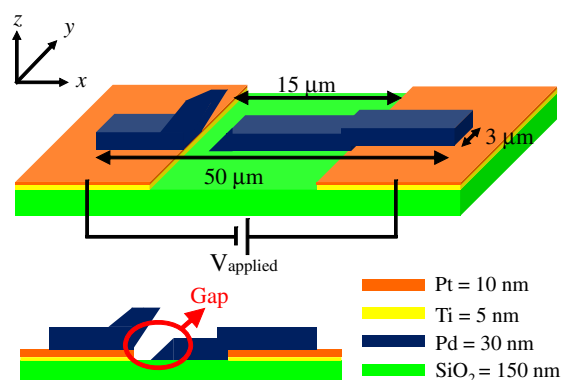
Figure 1. (a) Schematic plot of the explored 3D surface conduction electron-emitter (SCE) structure and cross-sectional plot of the SCE along the xz plane. The related thicknesses of materials are shown at the bottom on the right.

Figure 2. A simulated hydrostatic stress distribution in the realistic SCE structure after hydrogenation treatment. The maximal stress occurs around the step edge and this region is for crack formation.

PIC) calculation is performed for a self-consistent solution of the electromagnetic fields and charged particles. This enables us to explore electron emission properties with one Pd electron-emitter. In the field-emission process, electron emission is modeled by the Fowler–Nordheim (F–N) equation [10], where the conduction mechanism of the new device is explained. The field-emission characteristics of an SED device are significantly affected by material and geometric factors, including the work function of emitter materials, the separation of the nanogaps, and the morphology of the edge surfaces of the emitters. The electron conduction characteristics of a nanogap in different situations are further determined.

2. Experiment and simulation

A conventional nanogap in the SCE device is fabricated in palladium oxide electrodes prepared by ink-jet printing. To produce the nanogap, a pulse voltage is applied to the circular PdO film in vacuum, and then the PdO film is reduced to Pd by heating. Furthermore, it is split along the diameter and the submicron nanogap is formed, followed by the so-called activation process to deposit a chemical vapor deposition carbon layer on the Pd electrode to narrow the fissure to nanometer scale.

In this experiment, we employ a novel technique which has recently been developed to form the nanogap [9]. The Pd nanogap is fabricated on a p-type silicon wafer. The configuration of the new type of SCE and the cross section of nanogap device in this study are shown in figure 1. The silicon wafer is first thermally oxidized to form a SiO_2 insulator layer that is 150 nm thick, and then the pattern of the platinum (Pt) electrode is defined by photolithography process. Then 5 nm-thick titanium (Ti) and 10 nm-thick Pt thin films are sequentially deposited on the wafer by electron-beam evaporation deposition. A lift-off process is carried out to deposit a Pd strip that is 30 nm thick, 3 μm wide and 50 μm long. The Pd/Pt/Ti stacked structure on the SiO_2 wafer is then placed in a gas cell for the high-pressure hydrogen absorption treatment. During the absorption treatment, a hydrogen pressure in the cell of about 2×10^4 mbar embrittles the Pd and, after removing the hydrogen, the nanogap is
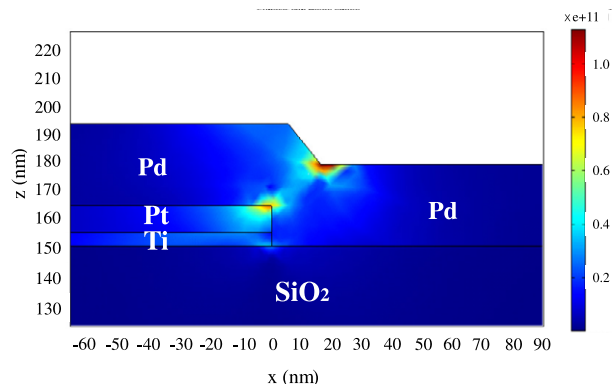
formed. Afterwards, a lift-off photolithography process is performed again to deposit Ti (equal to 5 nm), Pt (10 nm) and Pd (30 nm) films on the other side, and thus the SCE structure is completed.

Once Pd is exposed to hydrogen gas, hydrogen atoms have a very small mass and size, and an accordingly large diffusion coefficient. Hence, adsorbed hydrogen atoms can quickly diffuse into the Pd lattice and occupy the interstitial site [11–13]. For a system under tensile stress, the defects are often near strain singular points such as step edges or crack tips. There, hydrogen accumulates preferentially in regions of extremely high local stresses, increasing ductility locally and allowing the system to relax by forming cracks [14, 15]. Figure 2 shows the stress distribution map of the cross section of the emitter structure subject to the hydrogen treatment at 300 K. In this figure, it is indicated that the maximal stress occurs near the step edge and the least stress appears on the top of the Pd layer. Before the point of fracture, there is a large number of defects, especially in regions saturated by hydrogen. These defects act as seeds for crack formation. On the microscopic scale, fracture proceeds in a ductile manner and occurs more reactively at higher temperature. The mechanism of forming the nanogap may be described by the stress-induced migration model, which is treated as a process of void growth and stress relaxation through atomic diffusion driven by a stress gradient [16, 17]. The void growth depends on many factors, including stress, atom diffusivity, effective modulus, as well as the temperature. Therefore, the separation and edge roughness of the nanogap is increased due to the enhanced void growth rate at higher temperature. Figure 3 shows the plane-view SEM images of the nanogap formed on three Pd electrodes at different hydrogen absorption temperatures. The nanogap formed at 300 K, shown in figure 3(a), is approximately 30 nm wide, and the two other nanogaps prepared at 480 and 580 K have approximate separations of 60 and 90 nm respectively, as shown in figures 3(b) and (c). We notice that the width of the nanogaps is highly controllable at a given temperature (about 5% variation between nine samples with a 30 nm nanogap). The scanning electron micrograph (SEM) image of the cross section of the nanogap which is prepared by a focused ion beam with a width of about 30 nm is shown in figure 4. The break in the Pd electrode incurs
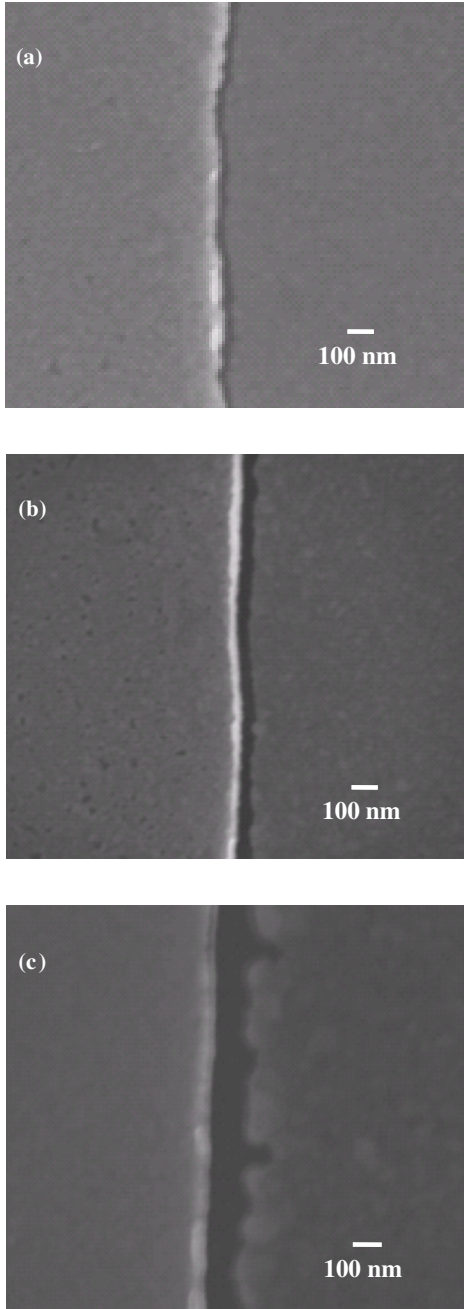
Figure 3. SEM images of the nanogaps formed on the Pd strips in the SCE structure at different hydrogen adsorption temperatures: (a) 25 °C, (b) 200 °C, and (c) 300 °C.

an extreme deformation around the geometric shape. The Pd electrode sticks out along the gap edge on the side with a Pt/Ti underlayer and exhibits a rugged feature on the other side with a gradual film thinning toward the edge. This observation clearly shows a vigorous cracking process accompanied by extensive atomic migration during the hydrogen treatment. By designing the geometric structure of the Pd electrode properly, we could successfully produce a single nanogap in the SCE device.

To explore the electron-emission properties in SCEs, the electromagnetic particle-in-cell scheme [18–20] is used;
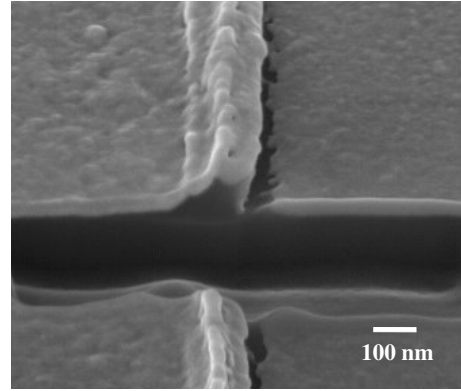
Figure 4. The SEM image of the cross section of the palladium nanogap with separation of approximately 30 nm.

starting from a specified initial state, we evaluate the electrostatic field along the emitter surface which is determined for a given geometry and applied voltage. In the field-emission process, electron emission is modeled by the F–N equation [10],

$$J = \frac{AE^2}{\varphi t^2} \exp\left(\frac{-Bv(y)\varphi^{3/2}}{E}\right), \qquad (1)$$

where $A = 1.541 \times 10^{-6}$ A eV V^{-2} and B is a fitting parameter in our simulation that depends on the applied voltage and the width of the nanogap, E is the normal component of the electric field at the emitter surface, φ is the work function of the emission material, t^2 is approximately equal to 1.1, and $v(y) = 0.95 - y^2$ with $y = 3.79 \times 10^{-5} \times E^{1/2}/\varphi$ in SI units. The emission current density is determined by equation (1) according to the local electric field, the work function of emitter material, and the fitting parameters. The weighted charge density and current density at the grids are subsequently calculated. The obtained charge density and current density are successively used as sources in the Maxwell equations for advancing the electromagnetic fields. We then perform a time integration of Faraday's law, Ampere's law, and the relativistic Lorentz equation [18],

$$\frac{\partial \mathbf{B}}{\partial t} = -\nabla \times \mathbf{E},$$
$$\frac{\partial \mathbf{E}}{\partial t} = -\frac{\mathbf{J}}{\varepsilon} + \frac{1}{\mu\varepsilon}\nabla \times \mathbf{B},$$
$$\mathbf{F} = q(\mathbf{E} + \mathbf{v} \times \mathbf{B}), \qquad \text{and} \qquad (2)$$
$$\frac{\partial \mathbf{x}}{\partial t} = \mathbf{v},$$

subject to constraints provided by Gauss's law and the rule of divergence of **B**,

$$\nabla \cdot \mathbf{E} = \frac{\rho}{\varepsilon} \qquad \text{and} \qquad \nabla \cdot \mathbf{B} = 0. \qquad (3)$$

We notice that **E** and **B** are the electric and magnetic fields, **x** is the position of a charged particle, and **J** and ρ are the current density and charge density resulting from charged particles. The full set of Maxwell's time-dependent equations is solved
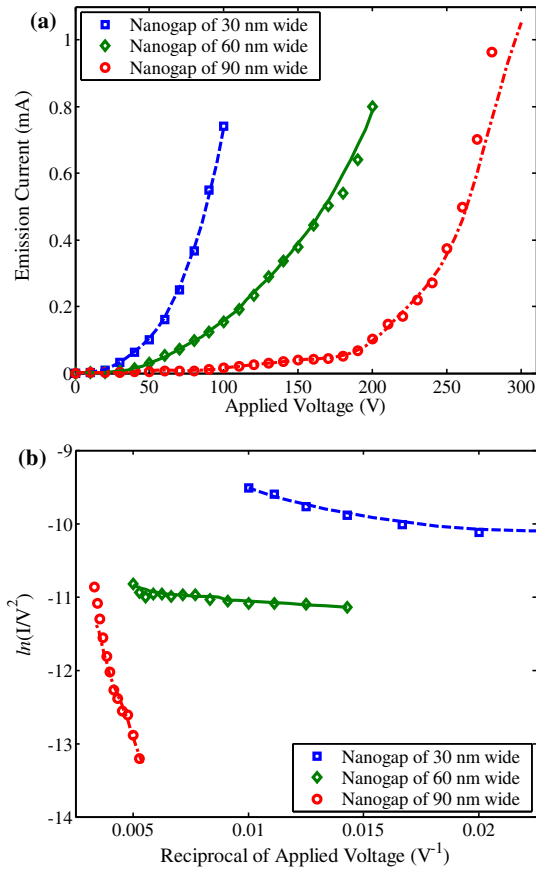
Figure 5. (a) The *I–V* characteristics of the SCE device with different gap widths. (b) The corresponding F–N plot, indicating the true nature of field emission. The solid lines are the experiment and the symbols are the simulation using the calibration model.

numerically to obtain the electromagnetic fields. Similarly, the Lorentz force equation is solved to obtain the relativistic particle trajectories. The charged particles move according to the Lorentz equation using the fields advanced in each time step. These steps are repeated for each time step until the specified number of time steps is reached. We notice that the space-charge effects [21] are automatically included in the solution procedure. This 3D FDTD-PIC thus approaches self-consistent simulation of the electromagnetic fields and charged particles.

3. Results and discussion

The simulated results are calibrated with the measured data before analyzing different structures. All surfaces in the simulation are assumed to be smooth on the cell level, but the surfaces of a nanogap may be extremely rough. For exploring the effects of the applied voltages and the widths of nanogaps upon the emission current, we study the electric field distributions around the nanogap. To compensate for roughness effects, we use one of the controls associated with the particular emission model. This approach is trying to gather from experimental data the electron yield ratio for smooth versus rough surfaces, and then adjust one of the yield parameters.

Figure 5(a) shows the measured and simulated current–voltage (*I–V*) characteristics with respect to different widths of nanogap when the applied voltage varies from 10 to 300 V, where the solid lines indicate the experimental data and the symbols are the simulated data. It is found, as shown in figure 5(a), that the turn-on voltage of 40 V is obtained at an emission current of 62 μA for a nanogap that is 30 nm wide. Two different turn-on voltages near 100 and 200 V are observed in the 90 nm nanogap. This phenomenon is caused by the Pd–H system reacting vigorously when the void growth rate is increased at higher temperature, such that the separation and edge roughness of the nanogap are enlarged. We can that see the edge of the nanogap in figure 3(c) is indeed more rugged than figures 3(a) and (b). Parts of the width of the nanogap in figure 3(c) may be shorter than 90 nm. Hence, when the applied voltage is up to 100 V, the first turn-on voltage is found due to conduction of the nanogap with the the shorter-separation part, and then the full region will turn on until the applied voltage attains the highest value, which is near 200 V in this case. There are at least two reasons why we cannot find two turn-on voltages at nanogap widths of 30 and 60 nm. The first is that the surfaces for these two cases are no rougher than the 90 nm nanogap — see figure 3—so the influence of surface roughness is insignificant in the narrower nanogap. The other reason is that, when the nanogap becomes narrower, it produces a very high electric field. The high electric field narrows the potential barrier at the metal–vacuum interface sufficiently for the electrons to have a chance of tunneling from the solid into vacuum. Therefore, electrons are injected entirely as the voltage reaches the critical value, and we can only observe one turn-on voltage for the 30 and 60 nm nanogap widths. A very high electron emission current of 0.1 mA is estimated at an applied voltage of 80 V for an emitter that is 60 nm wide. The corresponding F–N plot (i.e. a plot of $\ln(I/V^2)$ versus $1/V$) of the field emission of a Pd SCE is shown in figure 5(b). Assuming that the work function $\varphi = 5.12$ eV for Pd [22], the linear relationships in the high-voltage region indicate that the electron conduction followed the F–N field emission mechanism. However, the model of the bulk metal and its surface in F–N theory is restricted. The F–N theory considers the one-dimensional (1D) problem with a potential profile that only accounts for the image force. Thus, the atomic-scale surface roughness and the variation in the work function between different faces do not result in a significant deviation from the results obtained with the one-dimensional approximation [23]. In addition, the influence of emitter nonplanarity on the barrier shape was reported by He *et al* [24]. For the nonplanar model, the parameter *B* in equation (1) is modeled by a function of the field strength, as shown in figure 6. This results in the modified current density increasing slowly with the applied voltage, and its magnitude is greater than the current density for the planar model at the same voltage.

When the applied voltage is fixed at 60 V, the electric field contours with nanogap widths of 30, 60 and 90 nm are shown in figure 7, respectively. The local electric field near the nanogap, shown in figure 7(a), is higher than in figures 7(b) and (c). Therefore, the emission current in figure 7(a) should be higher than in figures 7(b) and (c). This novel structure, which has a different height between the two electrodes, implies that it
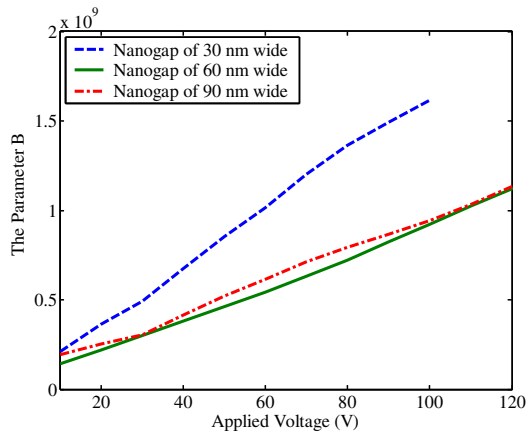
Figure 6. Plot of parameter *B*, shown in equation (1), versus the electric field with respect to different nanogap widths.

can produce high electric fields around the emitter apex, and generate a high emission current. It also has a protrusion on the cathode and an inclined sidewall, and these features can protect emission areas from being damaged by impurity ions during field-emission operation. In addition, the proposed nanogaps show the high field emission efficiency, compared with a conventional SCE device [25]. We observe, for the novel SCE, that the turn-on voltage is 40 V, which is substantially lower than that of the conventional 30 nm nanogap (it turns on at 60 V). For the 90 nm nanogaps, the turn-on voltage of field emission is about 100 V for the new structure and 170 V for the old structure.

The emission current in the SCE depends significantly on the thickness of the electrodes. By using the calibrated model, we further study the effect on field emission for different thicknesses and work functions of thin film simultaneously. Figure 8(a) shows a log plot of the characteristics of emission current versus the thickness of emitters with an applied voltage of 60 V. The simulation result shows that the changing rate of emission current is larger when the width of the nanogap is smaller in the thin thickness region. However, when the thickness of the emitter is increased, the emission current approaches a saturation region. This phenomenon is also obtained by equation (1) and figure 6 due to a higher slope in the narrower case. Figure 8(b) shows the corresponding electron charge for field emission with three nanogap widths. The electron charge, as shown in figure 8(b), increases towards the saturation region in the smaller nanogap when the thickness increases. Therefore, this reflects that the influence of thin-film thickness on field emission is more important for smaller nanogaps.

High brightness and long lifetime are the main targets of emission material investigations for scientific instrument applications, but high current density and low power consumption are the guiding rules for display applications. Hence, here we have explored the emission characteristics caused by different material work functions with respect to different nanogap widths, because changes in the local work functions lead to field-emission current fluctuation [26]. A log plot of the emission current as the work function varyies from 3.9 to 5.6 eV is shown in figure 9(a) with an applied
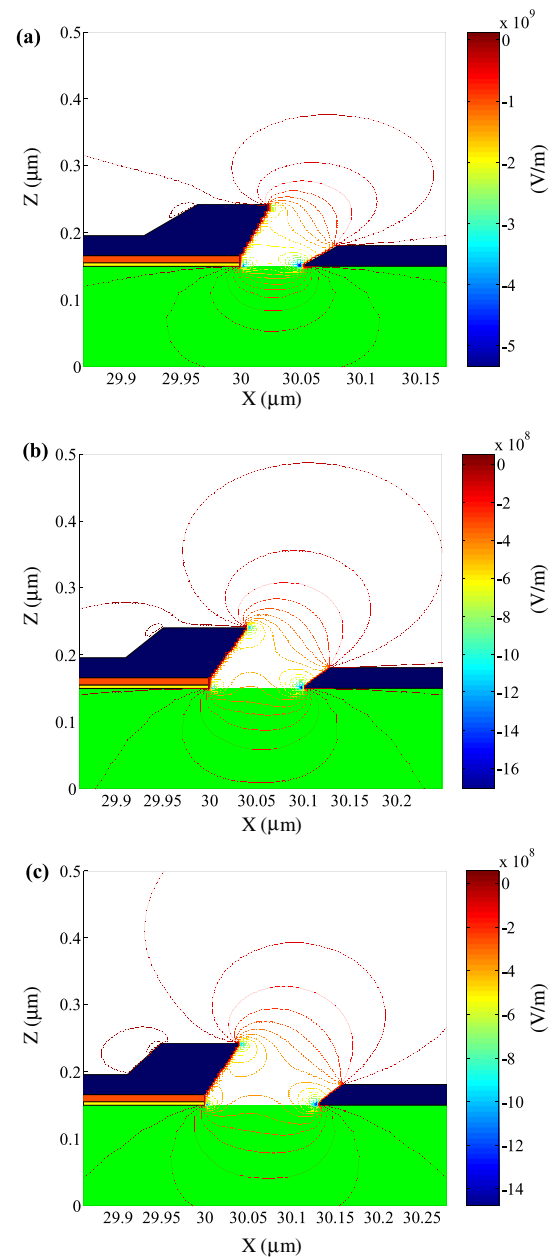
Figure 7. Contour plots of electric fields with different widths of nanogaps: (a) 30 nm, (b) 60 nm, and (c) 90 nm, respectively. The applied voltage is fixed at 60 V.

voltage of 60 V and an emitter that is 30 nm thick, where figure 9(b) shows the related electron charge for field emission. The simulation results show that a lower work function leads to higher emission current, and that the emission current takes on a linear distribution. The slope, shown in figure 9, is constant and does not depend on the width of the nanogap. When the work function of the material is changed from 5.12 to 4.82 eV, the emission current increases approximately two-fold, regardless of the width of the nanogap. Therefore, a decreased work function on the surface of a nanogap may increase the emission current. A change in local work function can be attained by hydrogen plasma treatment or annealing methods. To sum up the results, we find that the smaller the

(a)

(b)
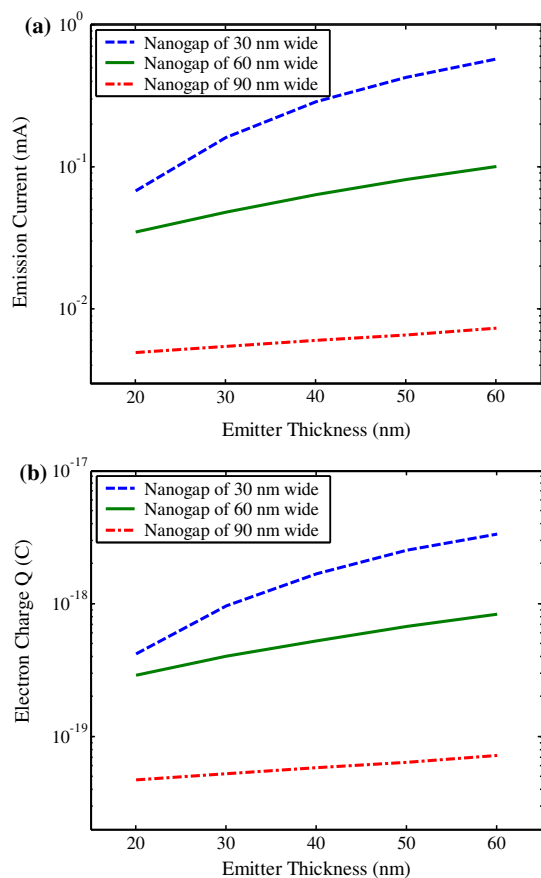
Figure 8. (a) Plot of emission current versus the thickness of the Pd strip electrode with different sizes of nanogap. (b) The corresponding electron charges for field emission in (a). All the results are calculated using the calibrated model.

(a)

(b)

Figure 9. (a) The effect of material work function on the field-emission current with various widths of nanogap. (b) The corresponding electron charges for the field emission in (a).

nanogap, the more prominent the emitter thickness is for the field emission capability. The variation in work function is proportional to the increase in emission current, while the latter is independent of the width of the nanogap.

4. Conclusions

We have successfully fabricated a single nanogap in a Pd strip electrode of a SCE structure by using high-pressure hydrogen absorption treatment. The current–voltage characteristics of this SCE have been studied and a turn-on voltage of 40 V is obtained at an emission current of 62 μA for a nanogap that is 30 nm wide. By using the calibrated model, electric field distributions are demonstrated for different nanogap widths. We have found that the change in emitter thickness has a slight influence on the emission current. However, modification of the material work function can significantly increase the emission efficiency. Consequently, the emission current can be increased by decreasing the gap width, increasing the emitter thickness, or decreasing the local work function. Using the proposed nanogap, it is also easy to build pairs of electrodes for making contacts to nanometer scale species, as well as for significant potential applications of the electron sources to field-emission displays.

References

[1] Reed M A, Zhou C, Muller C J, Burgin T P and Tour J M 1997 *Science* **278** 252–4
[2] Bezryadin A and Dekker C 1997 *J. Vac. Sci. Technol.* B **15** 793–9
[3] Yi M, Jeong K H and Lee L P 2004 *Biosens. Bioelectron.* **20** 1320–6
[4] Lee H I, Park S S, Park D I, Ham S H, Lee J H and Lee J H 1998 *J. Vac. Sci. Technol.* B **16** 762–4
[5] Nomura I, Sakai K, Yamaguchi E, Yamanobe M, Ikeda S, Hara T, Hatanaka K and Osada Y 1996 *Proc. IDW '96* pp 523–6
[6] Sakai K, Nomura I, Yamaguchi E, Yamanobe M, Ikeda S, Hara T, Hatanaka K, Osada Y, Yamamoto H and Nakagiri T 1996 *Proc. EuroDisplay '96* pp 569–72
[7] Yamaguchi E *et al* 1997 *J. Soc. Inf. Disp.* **5** 345–8

[8] Okuda M, Matsutani S, Asai A, Yamano A, Hatanaka K,
    Hara T and Nakagiri T 1998 *SID Symp. Digest* pp 185–8
[9] Tsai C H, Pan F M, Chen K J, Wei C Y, Liu M and
    Mo C N 2007 *Appl. Phys. Lett.* **90** 163115–7
[10] Fowler R H and Nordheim L W 1928 *Proc. R. Soc.* A
    119 173–81
[11] Lewis F A 1967 *The Palladium/Hydrogen System* (London:
    Academic)
[12] Wicke E and Brodowsky H 1978 *Hydrogen in Metals II*
    ed G Alefeld (Berlin: Springer)
[13] Zhong W, Cai Y and Tománek D 1992 *Phys. Rev.* B
    46 8099–109
[14] Zhong W, Cai Y and Tománek D 1993 *Nature* **362** 435–7
[15] Tománek D, Sun Z and Louie S G 1991 *Phys. Rev.* B
    43 4699–713
[16] Aoyagi M 2005 *J. Vac. Sci. Technol.* B **23** 2384–9

[17] Zhai C J and Blish R C 2005 *J. Appl. Phys.* **97** 113503–8
[18] Birdsall C K and Langdon A B 1985 *Plasma Physics via
    Computer Simulation* (New York: McGraw-Hill)
[19] Verboncoeur J P, Langdon A B and Gladd N T 1995 *Comput.
    Phys. Commun.* **87** 199–211
[20] Goplen B, Ludeking L, Smithe D and Warren G 1995 *Comput.
    Phys. Commun.* **87** 54–86
[21] Stern T E, Gosling B S and Fowler R H 1929 *Proc. R. Soc.* A
    124 699–723
[22] Michaelson H B 1977 *J. Appl. Phys.* **48** 4729–33
[23] van Oostrum A G J 1966 *Philips Res. Rep. Suppl.* **11** 1–102
[24] He J, Cutler P H and Miskovsky N M 1991 *Appl. Phys. Lett.*
    59 1644–6
[25] Tsai C H, Chen K J, Pan F M, Lo H Y, Li Y, Liu M and
    Mo C N 2007 *SID Symp. Digest* pp 583–5
[26] Yamamoto S 2006 *Rep. Prog. Phys.* **69** 181–232